OPEN ACCESS
IOP Publishing | International Atomic Energy Agency
Nuclear Fusion
Nucl. Fusion **64** (2024) 086007 (15pp)
https://doi.org/10.1088/1741-4326/ad521b

Divertor-safe nonlinear burn control based on a SOLPS parameterized core-edge model for ITER

Vincent Graber* **and Eugenio Schuster**

Department of Mechanical Engineering and Mechanics, Lehigh University, Bethlehem, PA, United States of America

E-mail: graber@lehigh.edu

Received 15 January 2024, revised 29 April 2024
Accepted for publication 30 May 2024
Published 18 June 2024

Abstract

For ITER operations, the range of desirable burning-plasma regimes with high fusion power output will be restricted by various operational constraints. These constraints include the saturation of ITER's various heating and fueling actuators such as the neutral beam injectors, the ion and electron cyclotron heating systems, the gas puffing system, and the deuterium–tritium pellet injectors. In addition to these actuator constraints, the H-mode power threshold, divertor detachment, and the heat load on the divertor targets may apply limitations to ITER's operational space. In this work, Plasma Operation Contour (POPCON) plots that map the aforementioned constraints to the temperature-density space are used to investigate which constraints are most limiting towards accessing regimes with high fusion power output. The presented POPCON plots are based on a control-oriented core-edge model that couples the nonlinear density and energy response models for the core-plasma region with SOLPS4.3 parameterizations for conditions in the edge-plasma regions (scrape-off-layer and divertor). Using this control-oriented core-edge model, a nonlinear burn controller, which aims to regulate the plasma temperature and density in the core-plasma region, is constructed in this work. This controller is augmented with an online optimization scheme that governs the control references such that the plasma can be guided towards regimes with high fusion powers while protecting the divertor targets from dangerously high heat loads. A closed-loop simulation study illustrates the capability of this burn control scheme.

Keywords: burn control, ITER, core-edge model, nonlinear kinetic control, operational constraints

(Some figures may appear in colour only in the online journal)

* Author to whom any correspondence should be addressed.

1. Introduction

The development of sophisticated algorithms that can regulate a burning plasma's temperature and density, which is the purpose of burn control, will be crucial for ITER's success [1]. Without effective burn control, alteration of the burn condition could result in undesirable transients. A model-based approach to burn control design [2–5] is advantageous because it directly incorporates the nonlinear and coupled dynamics of the plasma. Burn control is made more challenging due to the sensitivity of the core-plasma region to the edge-plasma regions and vice versa. For example, divertor detachment depends materially on the particle density and the total power balance in the core-plasma region. Moreover, achieving burn control objectives and protecting the divertor targets from high heat loads will need to be carefully balanced because an increase in the fusion reaction rate intensifies the power flowing into the scrape-off-layer (SOL) and onto the divertor targets. The peak heat load on ITER's tungsten (W) divertor should remain below 10 MW m^{-2} to avoid catastrophic melting [6]. While prior work used Lyapunov techniques [7] to design nonlinear burn controllers [8–10] from models of the core-plasma region, the burn condition can also be stabilized using artificial neutral networks that are developed using similar models [11].

A control-oriented model that couples the core region of burning deuterium–tritium (D–T) plasmas to the SOL and divertor regions is proposed in this work. This model is used to investigate desirable burning plasma regimes for D–T ITER operations and to develop a nonlinear burn control solution. In this model, the plasma's core region, which spans from the magnetic axis to the last-closed-flux-surface (LCFS), is governed by nonlinear, zero-dimensional response models for the plasma's density and temperature. These models balance the transport of particles and heat coming in and out of the plasma's core. Meanwhile, the edge-plasma region, which extends beyond the LCFS, is governed by scaling laws that were generated by parameterizing the results of high-fidelity SOLPS4.3 simulations of ITER [12]. SOLPS4.3 is a sophisticated plasma boundary transport code package, and the parameterized simulations were carried out for high-power, D–T operations with a full-tungsten divertor. Furthermore, the edge-plasma region was assumed to be seeded with either neon or nitrogen impurities. In this work, the core-plasma model and the edge-plasma scaling laws are coupled through the exchange of various parameters. The edge-plasma scaling laws determine the particle influx across the separatrix (including the D–T fuel) and the ion and electron separatrix temperatures that enter into the core-plasma model. The divertor target heat load and the degree of detachment are also determined by the scaling laws. These scaling laws depend on the power entering the SOL and the outflow of particles across the separatrix, which are determined by the core-plasma region's energy and density response models. The core-plasma actuators include auxiliary heating and pellet injection, and the edge-plasma actuators include gas fueling and particle pumping.

In prior work [13, 14], a core-SOL-divertor (CSD) model was developed by coupling the energy and density response models of the core-plasma region to a two-point model [15] of the SOL-divertor region (the model in [14] also included a neutral-particle response model for the divertor-plasma region). Similarly to the SOLPS4.3 parameterizations [12], the two-point model connects conditions at the separatrix to conditions near the divertor. In contrast to the model proposed in this work, the model in [14] relied on phenomenological quantities, such as the divertor retention time, which absorb many unknown relations (similarly to the global energy confinement time but without any widely used scaling laws that can be extrapolated to ITER and other future machines [16]). The values of these phenomenological quantities would have to be obtained by fitting the CSD model to either experimental data or transport simulations. By using parameterizations derived from high-fidelity SOL-divertor simulations of ITER, the model proposed in this work avoids this obstacle.

Fusion reactor performance can be evaluated using Plasma Operation CONtour (POPCON) plot analysis [17–19]. POPCON plots map plasma conditions, such as the fusion power output, over a space defined by two parameters, typically temperature and density. One approach to generating data for POPCON plots is to force a time-dependent transport code to sweep a region of temperature-density space using feedback control [20, 21]. This can be done by running several simulations, each with the density held at a different constant value, where the temperature is slowly increased such that the plasma is nearly at steady state throughout the simulation. The study of the ITER operation window presented in [6] was carried out using ASTRA, a high-fidelity core-transport code, with SOL-divertor scalings applied as boundary conditions. Alternatively, the differential equations describing the particle and energy balances can be solved at steady state ($\partial/\partial t = 0$) for a range of temperatures and densities [22]. This alternative approach is more suitable for zero-dimensional analysis. Even with the reduction in complexity, zero-dimensional POPCON plot analysis can be used to gleam characteristics of the burning plasma dynamics in a variety of future reactor designs [23].

ITER will need to push against operational limits to access desirable plasma regimes that maximize the fusion power output. In prior work [13, 24], control-oriented plasma models were used to generate POPCON plots that studied how the operational limits restrict the set of accessible burning plasma regimes (i.e. the ITER operable space). However, the plasma model used in [24] only considered the core-plasma region, and the core-edge plasma model used in [13] incorporated the two-point model (as described above) in place of the SOLPS4.3 parameterizations [12] used this work. In the POPCON analysis presented in this work, the operational limits not only include the Greenwald density limit and the maximum allowable heat load on the divertor targets but also the saturation of ITER's heating and fueling actuators. ITER's suite of actuators include two neutral beam injectors, the ion and electron cyclotron heating systems, two pellet injectors, and the gas fueling system [25]. Nonlinear burn control algorithms can make use of all of the aforementioned actuators to drive the plasma to the intended temperature and density.

Using the proposed core-edge plasma model, a divertor-safe burn control algorithm is developed in this work. By

applying Lyapunov techniques [7], control laws for the auxiliary heating and fueling are synthesized with the objective of driving the plasma system to a desired reference (e.g. a certain plasma energy and density). This controller is augmented with an algorithm that optimizes these references online, using the general approach outlined in [26–28], to satisfy certain performance targets and constraints. By minimizing a cost function, the references are optimized to direct the plasma system to targets for the electron temperature, electron density, and fusion power. These three targets were chosen because the POPCON plots presented in this work map isolines of the fusion power over the electron temperature-density space. To protect the divertor, the cost function includes a barrier function for the safety limit of the divertor heat load (10 MW m^{-2}), which is also mapped on the POPCON plots. Hypothetically, these POPCON plots can be employed to help determine desirable targets for the reference optimizer that approach without exceeding the actuator and operational constraints of the system. This approach to online reference optimization was previously used for burn control in [4], but the control algorithm in that work was based on a plasma model that was confined to the core-plasma region. The reference optimizer in this work is more suitable for divertor-safe ITER operation due to the inclusion of the SOLPS4.3 parameterizations, including a parameterization for the peak heat load on the divertor, in the plasma model. Unlike the core-only plasma model used in [4], the core-edge plasma model used in this work captures the impact of the core-plasma power balance, the ionic outflow of DT from the core-plasma region, the external gas puffing, and the impurity seeding on the divertor heat load.

This paper is organized as follows. In section 2, the proposed control-oriented core-edge model is presented as a core-plasma model coupled to the aforementioned SOLPS4.3 parameterizations. Section 3 provides an assessment of the ITER operable space based on POPCON plots. In section 4, the burn control objectives are given, the reference-tracking, nonlinear, burn controller is synthesized, and the online reference optimization scheme is devised. The simulation study in section 5 evaluates the performance of the proposed control scheme for divertor-safe burn control in ITER. Finally, conclusions are drawn and future work is proposed in section 6.

2. The core-edge burning plasma model

The core-edge model presented in this section is illustrated in figure 1, and it couples nonlinear energy and density response models for the core-plasma region to scaling laws for the edge-plasma regions (the SOL and divertor). The domain of the core-plasma model is the confined plasma bounded by the separatrix, while the SOL-divertor scalings, which are taken from SOLPS4.3 parameterizations of ITER burning plasmas [12], define the boundary of the core-plasma model and conditions at the divertor target. For example, the energy and density response models for the core-plasma region depend the separatrix ion and electron temperatures and the influx of particles across the separatrix (excluding the pellet injection that enters directly into the core-plasma region), respectively. Meanwhile, the outflow of the power and particles across the separatrix and into the SOL are inputs to the SOL-divertor scalings.

Burn control and divertor protection algorithms can be designed independently from each other, but the sensitivity between the core and edge regions of the plasma makes an integrated approach more attractive. Using auxiliary heating, pellet injection, gas puffing and pumping, divertor-safe burn controllers based on the presented core-edge model can drive a plasma to regimes with high fusion reaction rates (which is an output of the core-plasma model) while protecting the divertor from dangerously high heat loads (which is an output out the SOL-divertor scalings). The core-plasma (orange) and edge-plasma (purple) variables in figure 1 are defined in sections 2.1 and 2.2, respectively. Control algorithms can command the output of the actuators (magenta) during plasma operations. The presented model is designed to facilitate the synthesis of nonlinear controllers that use these actuators for integrated burn-divertor control.

2.1. The core-plasma model

With each term in units of W m^{-3}, the volume-averaged ion energy (E_i) and electron energy (E_e) response models in the core-plasma region are given by,

$$\dot{E}_i = -\frac{E_i}{\tau_{E,i}} + \phi_\alpha P_\alpha + P_{ei} + P_{aux,i}, \tag{1}$$

$$\dot{E}_e = -\frac{E_e}{\tau_{E,e}} + (1-\phi_\alpha) P_\alpha - P_{ei} - P_{rad} + P_{ohm} + P_{aux,e}, \tag{2}$$

where the fraction ϕ_α of the alpha-particle power P_α is deposited into the ion population, P_{ei} is the collisional energy exchange between the ion and electron populations, P_{rad} is the radiative losses, P_{ohm} is the ohmic heating, and the ion and electron energies have a confinement time of $\tau_{E,i}$ and $\tau_{E,e}$, respectively. All of the terms in (1) and (2), except for the controlled external heating ($P_{aux} = P_{aux,i} + P_{aux,e}$) from ITER's various auxiliary power sources, are dependent on the temperature of the plasma.

The ion and electron temperatures are assumed to have ITER-like parabolic profiles [29, 30]:

$$T_j(t,\psi) = (T_{j_0} - T_{j_s})(1-\psi/\psi_0)^2 + T_{j_s} \quad \text{for } j \in \{i,e\}, \tag{3}$$

where ψ and ψ_0 are the toroidal magnetic flux coordinate and the total flux enclosed at the separatrix, respectively. For $j \in \{i,e\}$, the temperature profiles are defined by a peaked central temperature T_{j_0} and a separatrix temperature T_{s_0} (see section 2.2 and appendix A). The volume average of (3) raised to the power k is defined as

$$\langle T_j(t)^k \rangle = \frac{1}{\psi_0 - 0} \int_0^{\psi_0} \left[(T_{j_0} - T_{j_s})(1-\psi/\psi_0)^2 + T_{j_s} \right]^k \mathrm{d}\psi \quad \text{for } j \in \{i,e\}. \tag{4}$$

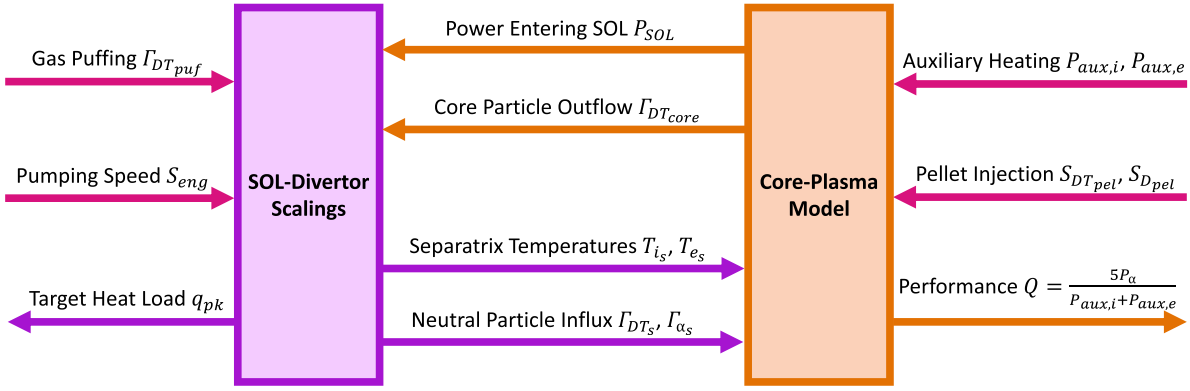

Figure 1. In the presented core-edge burning plasma model, the SOL-divertor scalings (purple) determine the peak heat load on the divertor targets, which must remain below a safety threshold to avoid catastrophic melting. In addition, the SOL-divertor scalings provide the following inputs to the core-plasma model: the ion separatrix temperature, the electron separatrix temperature, and the influx of particles (D, T, and α) across the separatrix. The core-plasma model (orange) determines the performance of the burning plasma (e.g. the ratio between the fusion power and the auxiliary power) along with the following inputs to the SOL-divertor scalings: the power entering the SOL and the outflow of particles across the separatrix. The actuators (magenta) that enter into the SOL-divertor scalings are the gas fuel puffing and the pumping speed, whereas the auxiliary heating (e.g. neutral beam injection) and the pellet fuel injection enter into core-plasma model.

The ion energy $E_i = \frac{3}{2} n_i \langle T_i \rangle$ and the electron energy $E_e = \frac{3}{2} n_e \langle T_e \rangle$ are dependent on the ion density n_i and the electron density n_e, respectively. For $k = 1$, the solution of (4) is $\langle T_j \rangle = \frac{1}{3} T_{j_0} + \frac{2}{3} T_{j_s}$ for $j \in \{i, e\}$. In comparison to the parabolic temperature profiles, the profile of the total plasma density ($n = n_i + n_e$) in ITER is expected be relatively flat [15, 29, 30]. Thus, the approximation $n(t, \psi) \approx n(t)$ is made in this work (similarly to the POPCON study in [22]). The plasma consists of four different species: deuterium with density n_D, tritium with density n_T, alpha particles with density n_α, and impurity particles with density n_z. Therefore, the ion density is $n_i = n_D + n_T + n_\alpha + n_z$. The quasi-neutrality condition (i.e. the number of electrons and protons in the plasma are equal) gives $n_e = n_D + n_T + 2n_\alpha + Z_z n_z$ where the impurity atomic number Z_z is either $Z_{Ne} = 10$ for neon or $Z_N = 7$ for nitrogen.

Because each D–T fusion reaction produces an alpha particle with $Q_\alpha = 3.52\,\text{MeV}$ of kinetic energy, the alpha-particle power is $P_\alpha = f_{loss} Q_\alpha S_\alpha$ where f_{loss} accounts for the effective percentage of alpha particles that escape confinement before they are fully thermalized. The reaction rate density is $S_\alpha = n_D n_T \langle \sigma \nu \rangle$ where the D–T reactivity is calculated using the parameterizations presented in [31]:

$$\langle \sigma \nu \rangle = G(T_{i_0}) \times C_1 \omega \sqrt{\xi / \left(m_r c^2 T_{i_0}^3\right)} e^{-3\xi}, \tag{5}$$

$$\xi = \left(B_G^2 / 4\omega\right)^{1/3},$$

$$\omega = T_{i_0} \left[1 - \frac{T_{i_0}\left(C_2 + T_{i_0}\left(C_4 + T_{i_0} C_6\right)\right)}{1 + T_{i_0}\left(C_3 + T_{i_0}\left(C_5 + T_{i_0} C_7\right)\right)}\right]^{-1}. \tag{6}$$

The constants $m_r c^2$, B_G, and C_j for $j \in \{1, \ldots, 7\}$ can be found in [31]. The correction factor $G(T_{i_0})$ from [22] is applied to account for the volume-averaging of the ion temperature profile.

In prior work [8], the following expression for the alpha power's ion-heating fraction [32, 33] was derived:

$$\phi_\alpha = \frac{1}{x_0}\left[\frac{1}{3}\ln\frac{1 - x_0^{\frac{1}{2}} + x_0}{\left(1 + x_0^{\frac{1}{2}}\right)^2} + \frac{2}{\sqrt{3}}\left(\arctan\frac{2x_0^{\frac{1}{2}} - 1}{\sqrt{3}} + \frac{\pi}{6}\right)\right], \tag{7}$$

where $x_0 = \varepsilon_{\alpha_0} / \varepsilon_c$ is the ratio between the alpha particle's initial kinetic energy ($\varepsilon_{\alpha_0} = Q_\alpha$) and the critical energy ε_c. As an alpha particle loses energy from collisions with the surrounding particles in the plasma, less of its energy is transferred to the electrons and more of it is transferred to the ions. At the critical energy,

$$\varepsilon_c = m_e^{-1/3} A_\alpha \frac{\langle T_e \rangle}{n_e^{2/3}} \left(\frac{3\sqrt{\pi} \ln \Lambda_i}{4 \ln \Lambda_e}\right)^{2/3} \left(\sum_{ions} \frac{n_i Z_i^2}{A_i}\right), \tag{8}$$

the alpha particle's kinetic energy is divided equally between the ions and electrons. In (8), the electron temperature is expressed in keV, $m_e = 9.1096 \times 10^{-31}\,\text{kg}$, the atomic mass is $A_\alpha = 4$, and the summation is taken over the plasma's four ion species (with $Z_D = Z_T = 1$ and $Z_\alpha = 2$). With the temperature expressed in K, the natural logarithm [34] is $\Lambda_k = 1.24 \times 10^7 \langle T_j^{3/2} \rangle / (n_e^{1/2} Z_{eff}^2)$ for $j \in \{i, e\}$ where the effective atomic number is given by $Z_{eff} = (Z_D^2 n_D + Z_T^2 n_T + Z_\alpha^2 n_\alpha + Z_z^2 n_z)/n_e$. For $k = \frac{3}{2}$, the solution of (4) is

$$\langle T_j^{3/2} \rangle = \frac{1}{4} T_{j_0}^{\frac{3}{2}} + \frac{3}{8} T_{j_s} \sqrt{T_{j_0}} + \frac{3}{8} \frac{T_{j_s}^2}{\sqrt{\Delta}} \ln\left(\sqrt{\Delta} + \sqrt{T_{j_0}}\right) - \frac{3}{8} \frac{T_{j_s}^2 \ln \sqrt{T_{j_s}}}{\sqrt{\Delta}} \quad \text{for } j \in \{i, e\}, \tag{9}$$

where $\Delta = T_{j_0} - T_{j_s}$.

The bremsstrahlung radiation losses and the ohmic heating [32] are given by

$$P_{rad} = 5.5 \times 10^{-37} Z_{eff} n_e^2 \langle T_e^{1/2} \rangle, \tag{10}$$

$$P_{ohm} = 2.8 \times 10^{-9} Z_{eff} I_p^2 a^{-4} \langle T_e^{-3/2} \rangle, \tag{11}$$

where T_e is in keV, and the plasma current and minor radius for ITER [16] are $I_p = 15$ MA and $a = 2$ m, respectively. The solutions to (4) when $k = \frac{1}{2}$ and $k = -\frac{3}{2}$ are

$$\langle T_j^{1/2} \rangle = \frac{1}{2}\sqrt{T_{j_0}} + \frac{T_{j_s}}{2\sqrt{\Delta}} \ln \left| \frac{\sqrt{\Delta^2 + \Delta T_{j_s}} + \Delta}{\sqrt{\Delta T_{j_s}}} \right|, \tag{12}$$

$$\langle T_j^{-3/2} \rangle = \frac{1}{T_{j_s}\sqrt{T_{j_0}}} \quad \text{for } j \in \{i, e\}. \tag{13}$$

The collisional exchange of power between the ions and electrons [34] is given by

$$P_{ei} = \frac{3}{2} n_e \frac{\langle T_e \rangle - \langle T_i \rangle}{\tau_{ei}}, \qquad \tau_{ei} = \frac{3\pi\sqrt{2\pi}\varepsilon_0^2 \langle T_e^{3/2} \rangle}{e^4 m_e^{1/2} \ln \Lambda_e} \sum_{ions} \frac{m_i}{n_i Z_i^2}, \tag{14}$$

where $e = 1.622 \times 10^{-19}$C and $\varepsilon_0 = 8.854 \times 10^{-12}$F/m. Similarly to the approaches taken in [13, 22], the volume average of P_{ei} was approximated in (14).

With each term expressed in units of m^3 s^{-1}, the alpha-particle (α), deuterium (D) and tritium (T) densities have the following response models:

$$\dot{n}_\alpha = -\frac{n_\alpha}{\tau_\alpha} + S_\alpha + \Gamma_{\alpha_s}, \tag{15}$$

$$\dot{n}_D = -\frac{n_D}{\tau_D} - S_\alpha + (1-\gamma)\Gamma_{DT_s} + S_D, \tag{16}$$

$$\dot{n}_T = -\frac{n_T}{\tau_T} - S_\alpha + \gamma\Gamma_{DT_s} + S_T, \tag{17}$$

where $\gamma = n_T/(n_D + n_T) = n_T/n_{DT}$ is the tritium fraction, S_D and S_T are the external fueling rates of D and T from pellet injection, and τ_D, τ_T and τ_α are particle confinement times. The particle influxes coming from the edge-plasma region Γ_{DT_s} and Γ_{α_s} are given by the SOLPS parameterizations discussed in section 2.2 and presented in appendix A. The outflow of fuel across the separatrix, which is an input to the SOLPS parameterizations, is given by

$$\Gamma_{DT_{core}} = \left(\frac{n_D}{\tau_D} + \frac{n_T}{\tau_T} \right) \times V, \tag{18}$$

where $V = 840$ m^3 is the ITER plasma volume [16]. The impurity concentration in the core-plasma region is assumed to be the constant $c_{z_{\text{core}}} = n_z/n_e$ for $z \in \{\text{Ne}, \text{N}\}$.

ITER is planned to be equipped with two pellet injectors. One of the injectors will be loaded with 100% deuterium pellets, while the other will be loaded with pellets that have a tritium fraction of $\gamma_{pel} = 90\%$. Respectively, the fueling rates of the two pellet injectors fuel are $S_{D_{pel}}$ and $S_{DT_{pel}}$. Because of the length of the guide tubes that will lead the pellets into the ITER vessel, the pellets are expected to lose approximately 10% of their mass ($C_{eff} = 90\%$) before entering the burning plasma [35]. Therefore, the external D and T fueling rates in (16) and (17) can be rewritten as

$$S_D = C_{eff} S_{D_{pel}} + C_{eff}(1 - \gamma_{pel}) S_{DT_{pel}}, \tag{19}$$

$$S_T = C_{eff} \gamma_{pel} S_{DT_{pel}}. \tag{20}$$

The global energy confinement time for H-mode plasmas [16] is

$$\tau_E = 0.0562 H I_p^{0.93} R^{1.97} B^{0.15} M^{0.19} \epsilon^{0.58} \kappa^{0.78} n_e^{0.41} P_{tot}^{-0.69}, \tag{21}$$

$$P_{SOL} \equiv P_{tot} = (P_\alpha + P_{aux} - P_{rad} + P_{ohm}) \times V, \tag{22}$$

where $P_{SOL} \equiv P_{tot}$ is the power entering the SOL in MW, H is the enhancement factor, $M = 3\gamma + 2(1-\gamma)$, and n_e is in units of 10^{19} m^{-3}. For ITER, the toroidal magnetic field is $B = 5.3$ T, the plasma major radius is $R = 6.2$ m ($\epsilon = a/R$), the vertical elongation at the 95% flux surface is $\kappa = 1.7$. The confinement times for the particles, the ion energy and the electron energy are proportional to τ_E such that $\tau_D = k_D \tau_E$, $\tau_T = k_T \tau_E$, $\tau_\alpha = k_\alpha \tau_E$, $\tau_{E,i} = \zeta_i \tau_E$, and $\tau_{E,e} = \zeta_e \tau_E$ where k_D, k_T, k_α, ζ_i, and ζ_e are constants. When the total plasma power (22) exceeds the power threshold P_{thresh} (MW), the plasma transitions from L-mode to H-mode [36]:

$$P_{thresh} = 4.3 M^{-1} B^{0.772} n_e^{0.782} R^{0.999} a^{0.975}. \tag{23}$$

2.2. The edge-plasma model

The core-plasma model presented in section 2.1 is coupled to SOLPS4.3 parameterizations [12] of the edge-plasma region. These parameterizations are listed in appendix A, and they define the following edge-plasma conditions: i—the neutral pressure μ (40) normalized to one at detachment ($\mu \leqslant 1 \rightarrow$ detached), ii—the peak heat load on the divertor targets q_{pk} (41), iii—the electron temperature at the separatrix T_{e_s} (42), iv—the ion temperature at the separatrix T_{i_s} (43), v—the influx of DT into the plasma's core from the edge-plasma region Γ_{DT_s} (44), and vi—the influx of helium into the plasma's core from the edge-plasma region Γ_{α_s} (45). These parameterizations are functions of the ionic outflow of DT fuel across the separatrix $\Gamma_{DT_{core}}$ (18), the power entering the SOL from the core-plasma region P_{SOL} (22), the seeded impurity concentration at the separatrix $c_{z_{sep}}$ (either neon or nitrogen), the engineering pumping speed S_{eng}, and the DT gas puffing rate $\Gamma_{DT_{puf}}$.

3. POPCON assessment of ITER's operable space

In this section, POPCON plots, which were generated by solving the control-oriented core-edge plasma model presented in section 2 at steady state ($d/dt = 0$), reveal the plasma regimes that are accessible to ITER under specific conditions. The methodology for generating the POPCON plots is similar to that explained in prior work [13], but the prior work did not use the SOLPS4.3 parameterizations discussed in section 2.2,

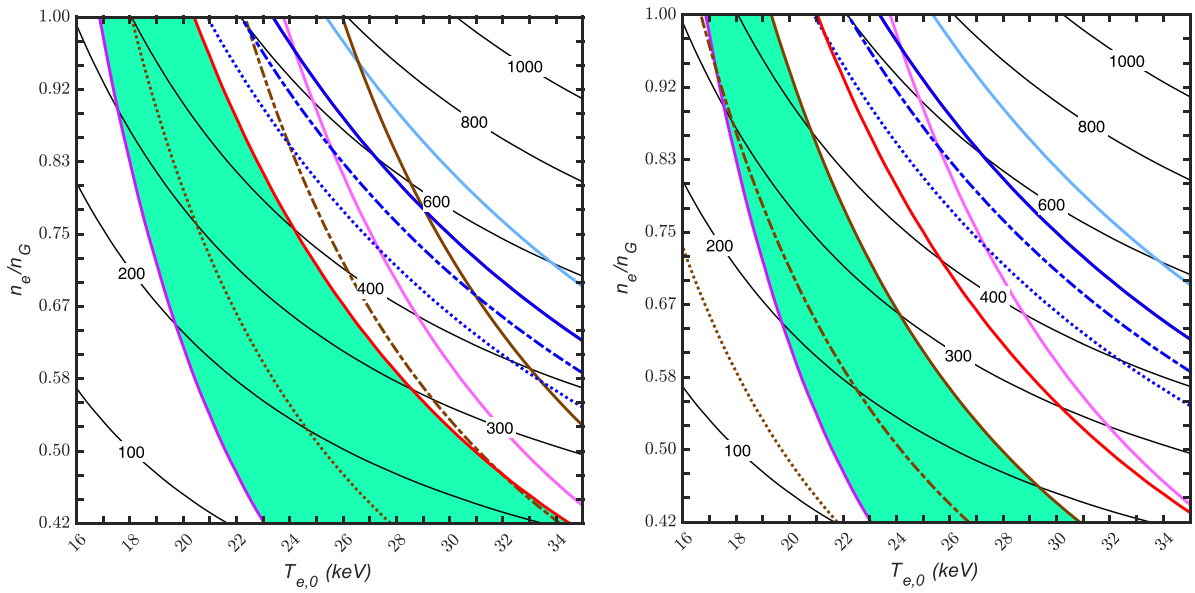

(a) $\mu = 1$ (b) $\mu = 1.4$

Figure 2. The two POPCON plots reveal steady-state conditions for ITER burning plasmas with a detached divertor ($\mu = 1$) and an attached divertor ($\mu = 1.4$). The solid black isolines map the fusion power in MW. The remaining solid isolines are operational limits: the auxiliary heating systems saturate (pink); the D pellet injector saturates (light blue); the D–T pellet injector saturates (dark blue); the gas fueling system saturates (brown); the divertor heat load exceeds the safety threshold (red); and the plasma is in H-mode (purple). The green area marks the space where all of the aforementioned operational limits are satisfied. Comparing the two plots, this green area in the density-temperature space shrinks as the normalized divertor pressure μ increases.

which can better predict the peak heat load on the divertor targets q_{pk} (41). More critically, the prior work did not consider the contribution of the DT gas puffing towards three important factors: (1) the overall plasma fueling, (2) the mitigation of the divertor heat load, and (3) the detachment of the divertor.

These POPCON plots, which are shown in figure 2, map the fusion power in MW (the solid-black contour lines) over a wide range of core-plasma electron temperatures ($T_{e,0}$) and electron densities (n_e). On the y-axis, the electron density is divided by the Greenwald density limit [37]

$$n_G = \frac{I_p}{\pi a^2}, \tag{24}$$

where n_G, I_p, and a are in units of 10^{20} m^{-3}, MA, and m, respectively. In addition to the fusion power, contour lines for the following ITER operational constraints [25, 36, 38] are plotted: i—the auxiliary heating systems saturate at 110 MW (solid pink), ii—the 100%D pellet injector saturates at 120 Pa m^3 s^{-1} (solid light blue), iii—the 10%D–90%T pellet injector saturates at 111 Pa m^3 s^{-1} (solid dark blue), iv—the gas fueling system saturates (reaches peak throughput) at 400 Pa m^3 s^{-1} (solid brown), v—the peak heat load on the divertor targets reaches the safety limit of 10 MW m^{-2} (solid red), and vi—the total plasma power exceeds the L–H power threshold such that the plasma is in H-mode (solid purple). The region in the temperature-density space where all six of the aforementioned constraints are satisfied is colored light green. This light green region indicates the operable space for the specific plasma plotted in the POPCON, and it reveals which constraints prevent access to plasma regimes with higher fusion powers.

In regard to pellet injection, the T concentration in the fueling lines, which can vary during long pulses, should remain high enough to replenish the T ion population and sustain the plasma's burn rate [24, 39]. Because adequate core-plasma T fueling is critical for ITER operations, additional saturation contour lines are shown (in figure 2) for the D–T pellet injector when the T concentration of the pellets are at 80% (dash-dot dark blue) and 70% (dotted dark blue). These additional contour lines show that the green operable space can shrink with decreasing T concentrations in the fueling lines. Also, additional contour lines are shown for when the gas fueling system's throughput is at 300 Pa m^3 s^{-1} (dash-dot brown) and 200 Pa m^3 s^{-1} (dotted brown).

The POPCON plots in figure 2 assume identical plasma conditions (e.g. both have a separatrix neon concentration of 0.4%) but different divertor conditions. In figure 2(a), a detached divertor ($\mu = 1$) is assumed, while an attached divertor ($\mu = 1.4$) is assumed in figure 2(b). In comparison to the plasma with an attached divertor (figure 2(b)), the plasma with a detached divertor (figure 2(a)) has a larger operable space (the light green region) and access to higher fusion powers (the solid-black contour lines). The L–H power threshold (the solid-purple contour line) acts as a lower bound on the operable space, while the rest of the operational constraints are upper bounds.

For the plasma with a detached divertor ($\mu = 1$) shown in figure 2(*a*), the most restrictive constraint is the maximum allowable heat load on the divertor (the solid-red contour line). This result emphasizes the importance of including divertor protection protocols in the design of burn control algorithms (see section 4.3). In contrast, the most restrictive constraint for the plasma with an attached divertor ($\mu = 1.4$) is the saturation of the gas fueling system (the solid-brown contour line) as shown in figure 2(*b*). As μ increases from 1 to 1.4, the most restrictive constraint transitions from the maximum allowable divertor heat load to the saturation of the gas fueling system. Based on the SOLPS4.3 parameterizations for μ (40) and the divertor heat load q_{pk} (41), this is the expected result. An increase in μ demands more gas puffing ($\Gamma_{DT_{puf}}$ increases), and q_{pk} decreases with increasing μ. Because an increase of $\Gamma_{DT_{puf}}$ increases μ and decreases q_{pk}, DT gas puffing must be used judiciously to keep $\mu \leqslant 1$ and $q_{pk} \leqslant 10$ MW m^{-2} simultaneously.

4. The divertor-safe burn control scheme

The presented core-edge model enables the design of nonlinear controllers that can achieve burn-condition objectives while incorporating constraints dictated by safe divertor operation. For example, the plasma could be driven to high-fusion-power regimes, such as those plotted in figure 2, while ensuring that the heat load on the divertor does not become too intense. In section 4.1, the burn control objectives are drawn, and the control laws designed to achieve these objectives are presented in section 4.2. The online optimization scheme presented in section 4.3 updates the controller's references in real time such that the desired fusion power output can be achieved without threatening the integrity of the divertor.

4.1. Burn control objectives

For the system of energy and density response models (1), (2), (15), (16) and (17), the burn controller is designed to track the following references for the states of the system: $\bar{E}_i$, $\bar{E}_e$, $\bar{n}_\alpha$, $\bar{n}_D$ and $\bar{n}_T$. The errors in the reference tracking are defined by $\tilde{E}_i = E_i - \bar{E}_i$, $\tilde{E}_e = E_e - \bar{E}_e$, $\tilde{n}_\alpha = n_\alpha - \bar{n}_\alpha$, $\tilde{n}_D = n_D - \bar{n}_D$, and $\tilde{n}_T = n_T - \bar{n}_T$. The burn control objective is to drive the deviations in the error system,

$$\dot{\tilde{E}}_i = -\frac{\bar{E}_i + \tilde{E}_i}{\tau_{E,i}} + \phi_\alpha P_\alpha + P_{ei} + P_{aux,i}, \tag{25}$$

$$\dot{\tilde{E}}_e = -\frac{\bar{E}_e + \tilde{E}_e}{\tau_{E,e}} + (1-\phi_\alpha) P_\alpha - P_{ei} - P_{rad} + P_{ohm} + P_{aux,e}, \tag{26}$$

$$\dot{\tilde{n}}_\alpha = -\frac{\bar{n}_\alpha + \tilde{n}_\alpha}{\tau_\alpha} + S_\alpha + \Gamma_{\alpha_s}, \tag{27}$$

$$\dot{\tilde{n}}_D = -\frac{\bar{n}_D + \tilde{n}_D}{\tau_D} - S_\alpha + (1-\gamma)\Gamma_{DT_s} + S_D, \tag{28}$$

$$\dot{\tilde{n}}_T = -\frac{\bar{n}_T + \tilde{n}_T}{\tau_T} - S_\alpha + \gamma\Gamma_{DT_s} + S_T, \tag{29}$$

to zero using the following four control inputs: the external ion heating $P_{aux,i}$, the external electron heating $P_{aux,e}$, the external deuterium fueling S_D, and the external tritium fueling S_T.

4.2. The burn controller

In this work, the following control laws for the external ion heating $P_{aux,i}$, the external electron heating $P_{aux,e}$, the external deuterium fueling S_D, and the external tritium fueling S_T are derived using Lyapunov techniques:

$$P_{aux,i} = \frac{\bar{E}_i}{\tau_{E,i}} - \phi_\alpha P_\alpha - P_{ei}, \tag{30}$$

$$P_{aux,e} = \frac{\bar{E}_e}{\tau_{E,e}} - (1-\phi_\alpha) P_\alpha + P_{ei} + P_{rad} - P_{ohm}, \tag{31}$$

$$S_D = \frac{1}{2}\left[3\frac{n_\alpha}{\tau_\alpha} + 2\frac{n_D}{\tau_D} + 2\frac{n_T}{\tau_T} + S_\alpha - 2S_T - 2\Gamma_{DT_s} - 3\Gamma_{\alpha_s} - (Z_z+1)\, c_{z_{core}} \dot{n}_e - K_N \tilde{n}\right], \tag{32}$$

$$S_T = \frac{n_T}{\tau_T} + S_\alpha - \gamma\Gamma_{DT_s} - K_T\tilde{\gamma} + \frac{\gamma}{2} \times \left[3\left(\frac{n_\alpha}{\tau_\alpha} - S_\alpha - \Gamma_{\alpha_s}\right) - (Z_z+1) c_{z_{core}} \dot{n}_e - K_N \tilde{n}\right], \tag{33}$$

where K_N and K_T are positive constants. The formulation of these control laws and the stability analysis of the system are provided in appendix B.

To successfully track the references, the burn controller's requests for external heating, control laws (30) and (31), and external fueling, control laws (32) and (33), must be precisely met with the suite of actuators available to ITER. For plasma heating in particular, the power output of ITER's ion cyclotron systems, electron cyclotron systems, and neutral beam injectors must be properly coordinated so that the power deposition is properly distributed between to the plasma's ion and electron populations. The mapping between the power-producing actuators and the heating control laws $P_{aux,i}$ and $P_{aux,e}$ can be resolved using actuator allocation (also known as control allocation—see [40] for a survey). The actuator allocation problem for burn control has been investigated in prior work with a variety of different actuator allocator designs [8–10]. All of the actuator allocators presented in [8–10] were designed independently from the burn controller such that any of these actuator allocators can work immediately with the burn control scheme proposed in this work. Because the design of these actuator allocators would not change when applied to this work, actuator allocation is not included this work for brevity (and to avoid the repetition of prior work). A discussion on actuator allocation and actuator dynamics can be found in appendix C. Moreover, details on the design of a variety of actuator allocators for ITER burn control can be found in prior work [8–10].

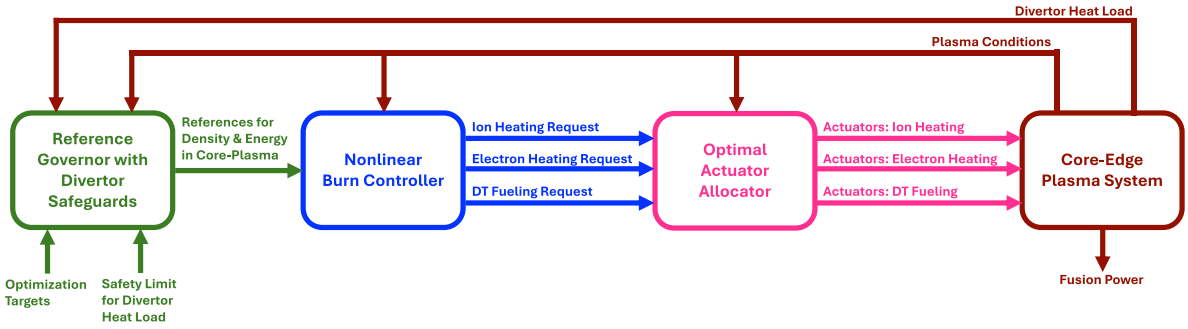

Figure 3. The reference governor optimizes the references for the burn controller ($\bar{E}_i$, $\bar{E}_e$, $\bar{n}$, and $\bar{\gamma}$) in order to achieve the chosen targets for the electron temperature ($T^p_{e_0}$), electron density (n^p_e), fusion power (P^p_{fus}), and tritium fraction (γ^p). After the burn controller receives the updated references, it sends out requests for external heating ($P_{aux,i}$ and $P_{aux,e}$) and fueling (S_D and S_T) to the actuator allocator, which maps the controller's requests to the available actuators. The external heating and fueling that is produced by the actuators evolve the core-edge plasma system. The loop is closed by feeding the plasma conditions, including the divertor heat load (q_{pk}), back to the different components of the burn control scheme. With the safeguards incorporated in the reference governor, the overall burn control scheme is designed to respect the integrity of the divertor.

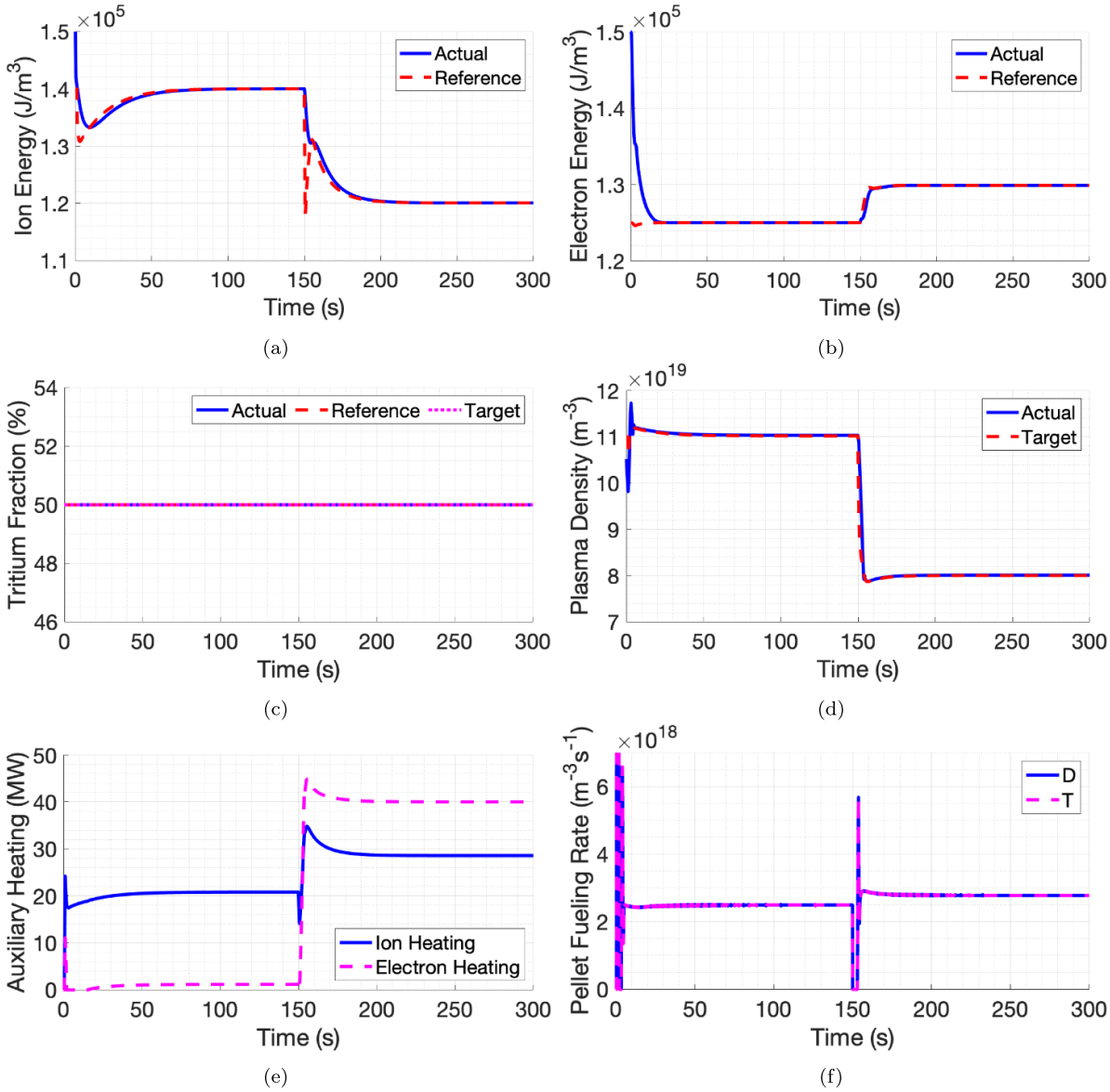

Figure 4. (*a*)–(*d*) The controller drives the states (blue-solid lines) to their reference values (dashed-red lines), which are updating over time due to the reference optimizer. (*e*) and (*f*) In order to achieve this, the controller commands the external heating and fueling rates provided by the actuators. [Scenario 1].

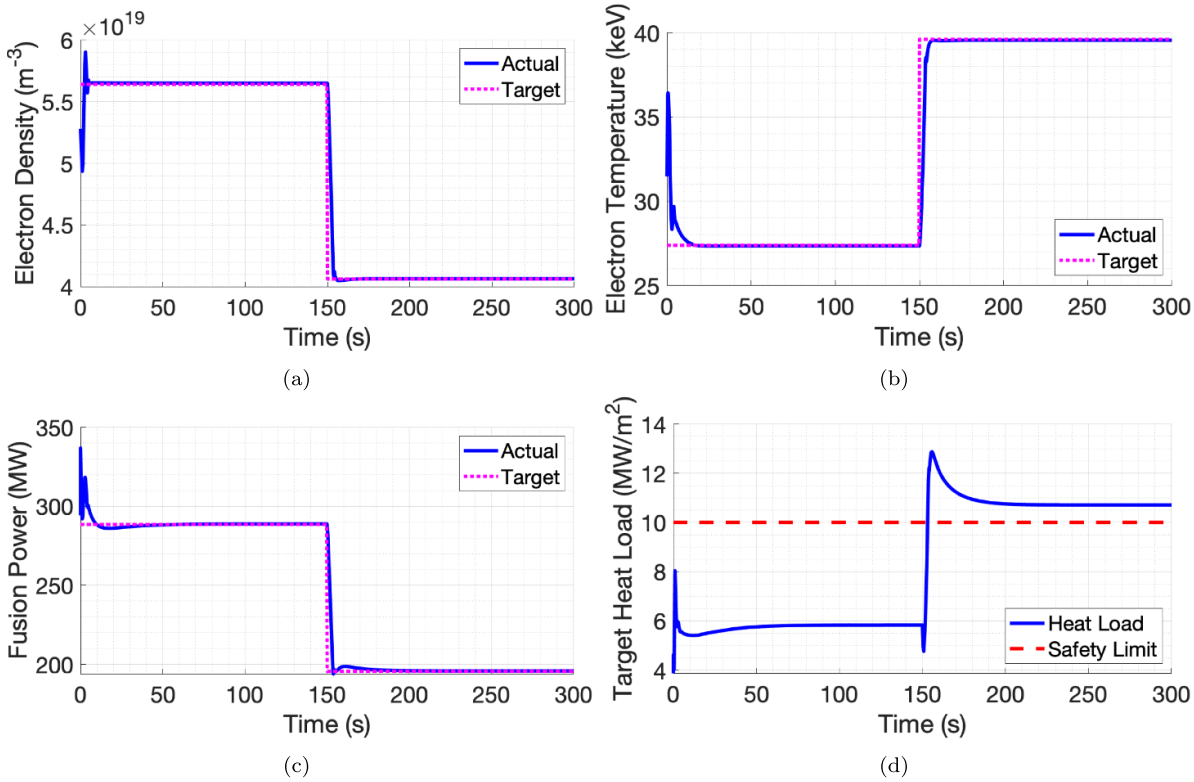

Figure 5. (*a*)–(*c*) The reference optimizer successfully directs the electron density, electron temperature, and fusion power (blue-solid lines) to their target values (magenta-dotted lines) by updating the references sent to the controller (see figure 4). (*d*) Because the reference optimization was unconstrained in this simulation, the peak heat load on the divertor targets exceeds the safety limit. [Scenario 1].

4.3. The reference optimizer

The objective of the burn controller presented in section 4.2 is to drive the system to the state references $r = [\bar{E}_i \quad \bar{E}_e \quad \bar{n} \quad \bar{\gamma}]^T$, which determine the plasma conditions (e.g. the electron temperature, electron density, alpha-particle power, energy confinement time, and so on) at steady state. This section addresses the problem of optimizing the references such that the desired targets for the plasma conditions, including the fusion power ($P_{fus} = 5 \times P_{\alpha}$), can be achieved without harming the divertor. This problem is resolved by inserting a divertor-safe reference governor into the closed-loop system as depicted in figure 3. After the reference governor (green) updates the references online, the burn controller (blue) sends out requests for external heating and fueling to the actuator allocator (pink). After the actuator allocator commands the various actuators to correctly output the required values for $P_{aux,i}$, $P_{aux,e}$, S_D, and S_T, the plasma system (red) evolves and moves towards the chosen optimization targets. With the constraint for the maximum allowable heat load on the divertor targets included in its design, the reference governor will only direct the plasma system towards divertor-safe regimes.

Using the following cost function, the reference governor directs the plasma system to the optimization targets (e.g. the desired fusion power) by updating the controller's references (r) in real time:

$$p(r,x^*) = \frac{w_1}{2}\left(T_{e_0} - T^p_{e_0}\right)^2 + \frac{w_2}{2}\left(n_e - n^p_e\right)^2 + \frac{w_3}{2}\left(P_{fus} - P^p_{fus}\right)^2 + \frac{w_4}{2}\left(\gamma - \gamma^p\right)^2 - w_5 \ln(-G), \tag{34}$$

where T_{e_0}, n_e, P_{fus}, γ, and G are calculated using r and $x^* = n_{\alpha}$. The optimization targets include the desired electron temperature $T^p_{e_0}$, the desired electron density n^p_e, the desired fusion power P^p_{fus}, and the desired tritium fraction γ^p. The target deviations are weighted with the constants w_1, w_2, w_3, and w_4. By selecting $G = q_{pk} - q^{\max}_{pk}$ where $q^{\max}_{pk} = 10$ MW m^{-2}, the barrier function in (34), which is weighted by w_5, is designed to protect the divertor from high heat loads. The cost function (34) can be modified to consider different targets (e.g. the ion temperature or the energy confinement time) and additional constraints (e.g. actuator saturation or the L–H power threshold). To ensure a unique minimum, the plasma system's states are assumed to be constrained within the region of interest over which (34) is locally convex.

Similarly to the methodology taken in [4, 26–28], the reference optimization scheme is formulated by choosing the Lyapunov function

$$V_r = \frac{1}{2}\left(\frac{\partial p(r,x^*)}{\partial r}\right)^T \frac{\partial p(r,x^*)}{\partial r}, \tag{35}$$

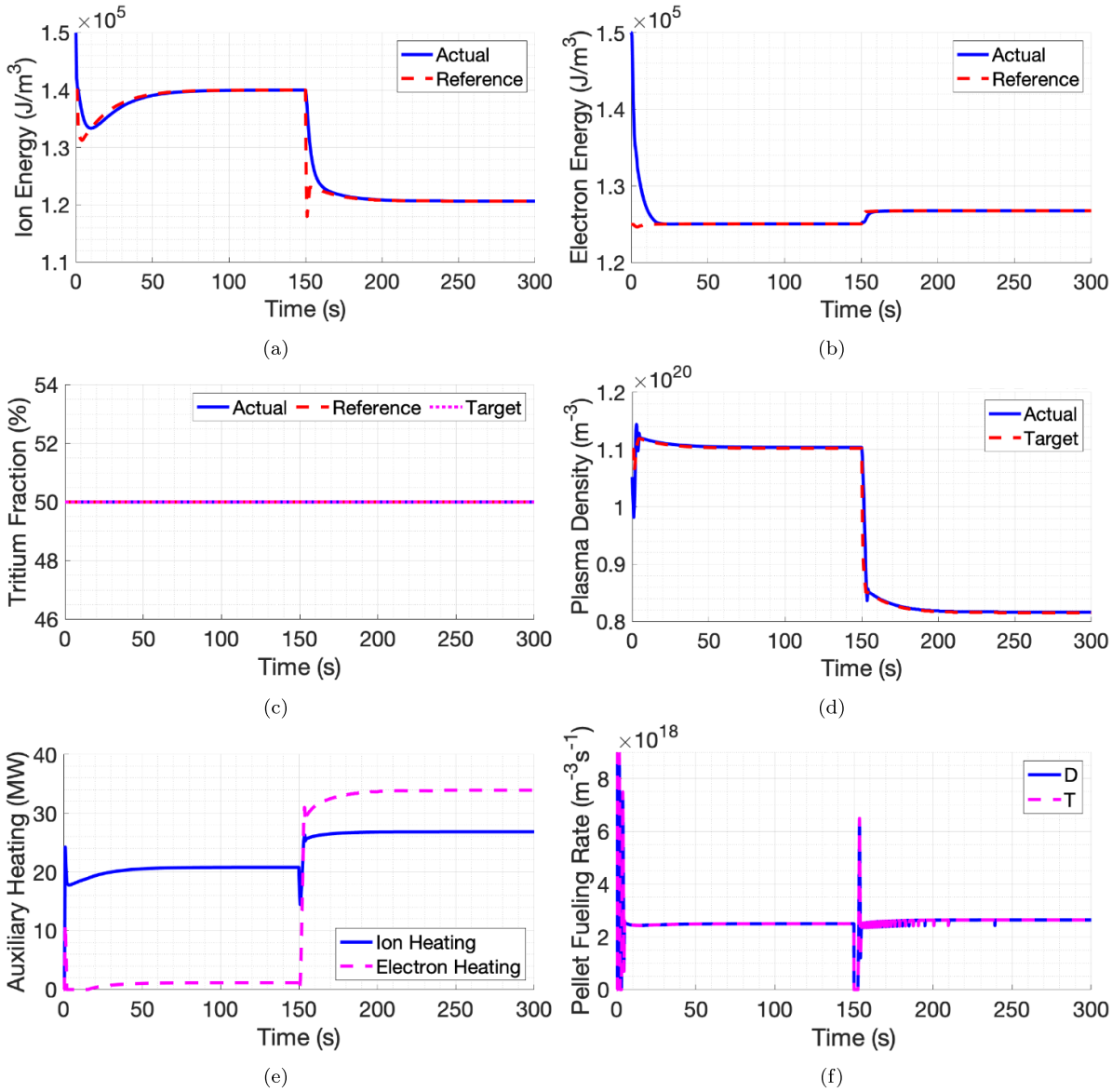

Figure 6. (*a*)–(*d*) The controller drives the states (blue-solid lines) to their reference values (dashed-red lines), which are updating over time due to the reference optimizer. (*e*) and (*f*) In order to achieve this, the controller commands the external heating and fueling rates provided by the actuators. [Scenario 2].

which has a time derivative of

$$\dot{V}_r = \left(\frac{\partial p}{\partial r}\right)^T \left[\frac{\partial^2 p}{\partial r^2}\dot{r} + \frac{\partial^2 p}{\partial r \partial x^*}\dot{x}^*\right]. \tag{36}$$

The reference update law

$$\dot{r} = -\left(\frac{\partial^2 p}{\partial r^2}\right)^{-1} \left[K_{opt}\frac{\partial p}{\partial r} + \frac{\partial^2 p}{\partial r \partial x^*}\dot{x}^*\right], \tag{37}$$

reduces (36) to

$$\dot{V}_r \leqslant -\left(\frac{\partial p}{\partial r}\right)^T K_{opt}\frac{\partial p}{\partial r}, \tag{38}$$

where K_{opt} is positive definite. Because this implies that $\frac{\partial p}{\partial r}$ is driven to zero, the reference update law (37) drives r to the the optimal value that respects the heat load constraints on the divertor. The inversion of $\frac{\partial^2 p}{\partial r^2}$ in the update law (37) requires that the reference optimizer's cost function (34) is convex in the region of interest. To avoid numerical issues, (37) can be replaced with

$$\dot{r} = -K_J\frac{\partial p}{\partial r} \quad \text{where} \quad K_J = K_{opt}\left\|\frac{\partial p}{\partial r}\right\|^{-\frac{1}{2}}, \tag{39}$$

when $\frac{\partial^2 p}{\partial r^2}$ is singular. The proposed reference optimizer is independent of the burn controller presented in section 4.2. Therefore, an alternative approach that relaxes the convexity requirement could be implemented in the future.

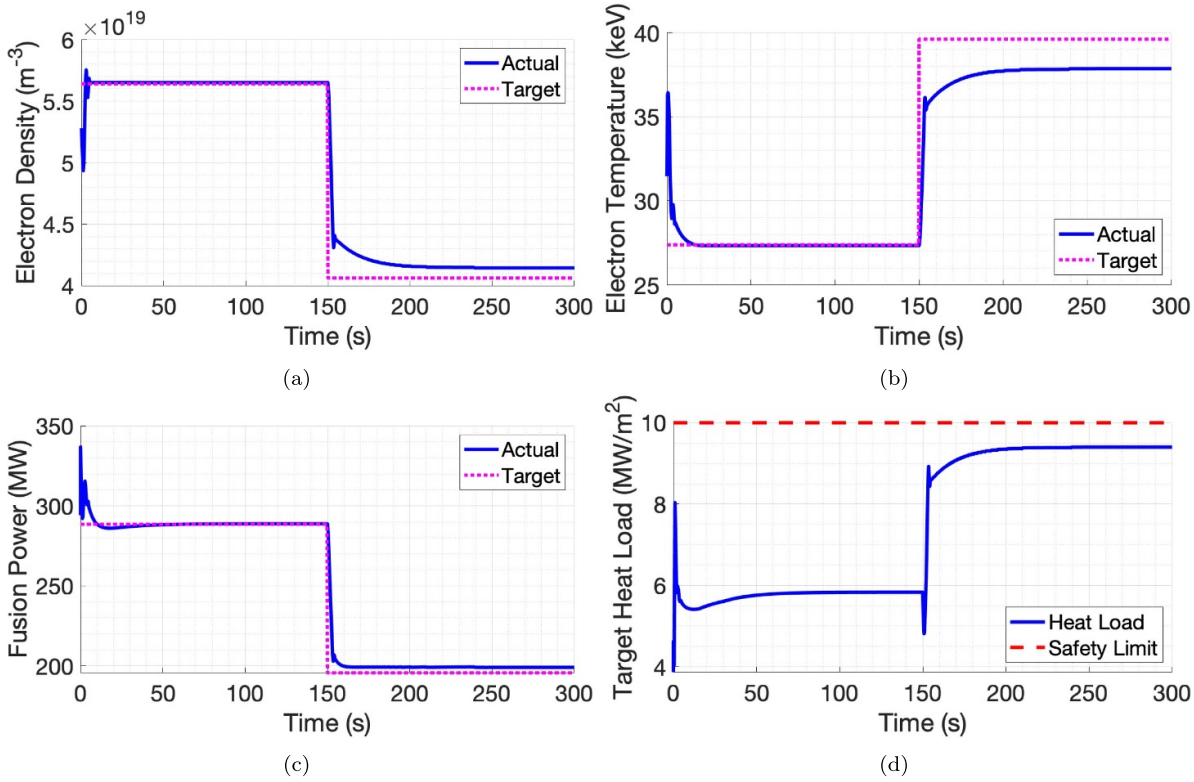

Figure 7. (*a*)–(*c*) The reference optimizer attempts to direct the electron density, electron temperature, and fusion power (blue-solid lines) to their target values (magenta-dotted lines) by updating the references sent to the controller (see figure 6). (*d*) Because the reference optimization was constrained in this simulation, the peak heat load on the divertor targets remain below the safety limit. For this reason, not all of the reference optimizer's targets are met. [Scenario 2].

5. Simulation study

In this section, the proposed divertor-safe burn control scheme is evaluated in closed-loop simulations of the core-edge plasma model (section 2). The control scheme consists of two components: (1) a controller (section 4.2) that tracks references for the ion energy, electron energy, plasma density, and tritium fraction; and (2) an online reference optimization scheme (section 4.3) that updates the references so that the controller drives the plasma to the chosen targets for the electron temperature, electron density, fusion power, and tritium fraction. In addition, the reference optimizer should keep the plasma away from targets that result in dangerously high divertor heat loads (i.e. keep q_{pk} under 10 MW m^{-2}). The simulation study consists of two scenarios. In the first scenario (shown in figures 4 and 5), the reference optimization is set to be unconstrained by setting $w_5 = 0$ in the cost function (34). In the second scenario (shown in figures 6 and 7) the reference optimization is set to be constrained ($w_5 \neq 0$) such that high heat loads on the divertor targets are avoided ($q_{pk}^{max} = 10$ MW m^{-2}).

The two scenarios share the following simulation settings. For the core-plasma region of the model, $H = 1$ $k_\alpha = 6$, $k_D = 3$, $k_T = 3$, $\zeta_i = 1.25$, $\zeta_e = 0.73$, and $f_{loss} = 1$. For the edge-plasma region of the model, $\Gamma_{DT_{puf}} = 70$ Pa m^3 s^{-1}, $S_{eng} = 65$ m^3 s^{-1}, and $c_{z_{sep}} = 0.4\%$ (neon). At the start of both simulations, the online reference optimization scheme was set to achieve the following four targets: $P_{fus}^p = 288.5$ MW, $T_{e_0}^p = 27.4$ keV, $n_e^p = 5.6 \times 10^{19}$ m^{-3}, and $\gamma^p = 0.5$. After 150 s, the optimizer's four targets were changed to be the following: $P_{fus}^p = 195.6$ MW, $T_{e_0}^p = 39.6$ keV, $n_e^p = 4.1 \times 10^{19}$ m^{-3}, and $\gamma^p = 0.5$.

Figures 4 and 5 show the simulation results of Scenario 1 where the reference optimization scheme is unconstrained. Using external heating and fueling ($P_{aux,i}$, $P_{aux,e}$, S_D, and S_T), the burn controller successfully tracks the references ($\bar{E}_i$, $\bar{E}_e$, $\bar{n}$, and $\bar{\gamma}$) despite them changing over time due to the reference optimizer (figure 4). By updating the control references over time, the reference optimizer successfully directs the system to the target electron temperature, electron density, and fusion power despite these targets changing at 150 s (figure 5). Because the optimizer in Scenario 1 is unconstrained, the heat load on the divertor targets exceeds the safety limit. Unlike Scenario 1, the optimization scheme is constrained in Scenario 2 by activating the barrier function in the cost function (34) (i.e. $w_5 \neq 0$), which protects the divertor targets from intense heat loads. In Scenario 2, the burn controller successfully tracks the references (figure 6), but because the divertor heat load approaches the safety limit after 150 s (when the optimizer's targets are changed), the reference optimizer redirects the control references such that the optimizer's targets are not achieved (figure 7). The optimizer prioritizes the protection of the divertor over the achievement of its performance targets.

6. Conclusions and future work

The presented model couples the energy and density response models for the core-plasma region to SOLPS4.3 parameterizations of ITER's edge-plasma regions. Using this model, POPCON plots were generated to give insight on how various operational constraints, such as actuator saturation and maintaining H-mode, render portions of the temperature-density space inaccessible to specific burning plasmas. For future work, a more comprehensive POPCON study can be undertaken to analyze changes to the operable space under a wide swath of parameter variations. For example, variations in the enhancement factor or the separatrix impurity concentration may be investigated.

Burn control becomes more challenging once the divertor is taken into consideration because core-plasma and divertor-plasma objectives may conflict. For example, achieving higher fusion powers increases the power flowing into the SOL and intensifies the divertor heat load. The presented simulation study demonstrates that the proposed nonlinear burn control scheme can regulate the burning plasma system while the reference optimizer safeguards the integrity of the divertor. In the presented model, various parameters, such as the enhancement factor for the global energy confinement time, may not be well known ahead of ITER's operation. In addition, these uncertain parameters may vary between pulses. In prior work [8, 9], this parameter uncertainty was handled using adaptive control techniques, however the burn controllers were based on models that only included the core-plasma region. For future work, these adaptive control techniques may be used to design controllers based on the presented core-edge plasma model. Furthermore, zero-dimensional nonlinear burn controllers, such as the one proposed in this work, may be evaluated in one-dimensional simulations that evolve the spatio-temporal response of the plasma energy and density. Certain actuator dynamics, which will render burn control more challenging, can be better captured in one-dimensional space. This includes the discrete behavior of the pellet injectors and the localized response of the plasma density to pellet injection.

Acknowledgments

This material is based upon work supported by the U.S. Department of Energy, Office of Science, Office of Fusion Energy Sciences under Award Number DE-SC-0010661. This work was carried out in part under the ITER Scientist Fellow Network program.

Appendix A. SOLPS4.3 parameterizations

In [12], SOLPS4.3 simulations were carried out to establish the following scalings for 60 MW $< P_{SOL} <$ 120 MW at $c_{z_{sep}} = 0.4\%$ and $c_{z_{sep}} = 1.2\%$ and additionally for $0.2\% < c_{z_{sep}} \leqslant 1.8\%$ at $P_{SOL} = 100$ MW where $c_{z_{sep}}$ for $z \in \{\mathrm{Ne}, \mathrm{N}\}$ is the seeded impurity concentration at the separatrix. This simulation study defined the parameter μ as the neutral pressure normalized to one at detachment:

$$\mu = \left(\frac{\Gamma_{DT_{SOL}}}{250\bar{S}_{eng}}\right)^{0.83} \bar{P}_{SOL}^{-0.52}, \qquad (\mu \leqslant 1 \rightarrow \text{detached}), \quad (40)$$

where $\bar{P}_{SOL} = P_{SOL}\,[\mathrm{MW}]/100$, $\Gamma_{DT_{SOL}} = \Gamma_{DT_{core}} + \Gamma_{DT_{puf}}$ is the total D–T flux into the SOL (Pa m^3 s^{-1}), $\Gamma_{DT_{core}}$ is given in section 2.1, and $\Gamma_{DT_{puf}}$ is the controlled gas injection rate. The engineering pumping speed S_{eng} (m^3 s^{-1}) [41] is normalized to give $\bar{S}_{eng} = S_{eng}/57$. ITER's pumping system [25] can operate at speeds between 65 m^3 s^{-1} and 107 m^3 s^{-1}. The pumping speed can be modified in real-time, but the response time will be slow (around 5–10 s).

The divertor heat load q_{pk} (MW m^{-2}), which should remain below 10 MW m^{-2} to avoid melting, is given by

$$\begin{bmatrix} q_{pk}|^{\mathrm{Ne}} \\ q_{pk}|^{\mathrm{N}} \end{bmatrix} = \max\left(\begin{bmatrix} 4.01 \\ 3.45 \end{bmatrix} \bar{P}_{SOL}^{1.44}\,\mu^{-0.83}, \quad 5.819\bar{P}_{SOL}^{1.12}\,\mu^{-0.32} \begin{bmatrix} \bar{c}_{\mathrm{Ne}_{sep}}^{-0.29} \\ \bar{c}_{\mathrm{N}_{sep}}^{-0.19} \end{bmatrix}\right), \quad (41)$$

where $\bar{c}_{z_{sep}} = c_{z_{sep}}/0.004$ for $z \in \{\mathrm{Ne}, \mathrm{N}\}$. The electron and ion temperatures at the separatrix (eV),

$$\begin{bmatrix} T_{e_s}|^{\mathrm{Ne}} \\ T_{e_s}|^{\mathrm{N}} \end{bmatrix} = \bar{P}_{SOL}^{0.31}\left(\frac{\bar{P}_{SOL,e}}{\bar{P}_{SOL,i}}\right)^{0.05} \times \max\left(140\mu^{-0.093}\begin{bmatrix} \bar{c}_{\mathrm{Ne}_{sep}}^{0.046} \\ \bar{c}_{\mathrm{N}_{sep}}^{0.037} \end{bmatrix}, \quad 150\begin{bmatrix} \bar{c}_{\mathrm{Ne}_{sep}}^{0.092} \\ \bar{c}_{\mathrm{N}_{sep}}^{0.063} \end{bmatrix}\right), \quad (42)$$

$$\begin{bmatrix} T_{i_s}|^{\mathrm{Ne}} \\ T_{i_s}|^{\mathrm{N}} \end{bmatrix} = \bar{P}_{SOL}^{0.27}\left(\frac{\bar{P}_{SOL,e}}{\bar{P}_{SOL,i}}\right)^{-0.13} \times \frac{\max\left(200\mu^{-0.19}\begin{bmatrix} \bar{c}_{\mathrm{Ne}_{sep}}^{0.23} \\ \bar{c}_{\mathrm{N}_{sep}}^{0.12} \end{bmatrix}, \quad 230\bar{c}_{z_{sep}}^{0.105}\right)}{1 + 0.08\left(1 - \frac{\Gamma_{DT_{puf}}}{\Gamma_{DT_{SOL}}}\right)}, \quad (43)$$

depend on $P_{SOL,e} \equiv (1-\phi_\alpha)P_\alpha + P_{ohm} - P_{rad} - P_{ei} + P_{aux,e}$ and $P_{SOL,i} \equiv \phi_\alpha P_\alpha + P_{ei} + P_{aux,i}$. The neutral particle influxes

across the separatrix (Pa m^3 s^{-1}) for the DT fuel (Γ_{DT_s}) and the helium impurity (Γ_{α_s}) decrease with increasing P_{SOL}:

$$\begin{bmatrix}\Gamma_{DT_s}|^{\mathrm{Ne}}\\ \Gamma_{DT_s}|^{\mathrm{N}}\end{bmatrix} = \begin{bmatrix}\bar{c}_{\mathrm{Ne}_{sep}}^{0.86}\\ \bar{c}_{\mathrm{N}_{sep}}^{0.58}\end{bmatrix} 0.0053 \bar{P}_{SOL}^{-1.6}\,\mu^{-0.65}\bar{S}_{eng}^{-0.38}\,\Gamma_{DT_{SOL}} \times \left(1+0.25\left(1-\frac{\Gamma_{DT_{puf}}}{\Gamma_{DT_{SOL}}}\right)\right), \tag{44}$$

$$\Gamma_{\alpha_s} = 2\bar{P}_{SOL}^{-1}\,\mu^{-0.33}\bar{c}_{z_{sep}}^{0.35}\bar{S}_{eng}^{-0.93}\times(1.05P_\alpha/P_{SOL}) \times \max\left(0.0016\mu^{-1.9}\bar{c}_{z_{sep}}^{-0.35},\quad \min\left(\begin{bmatrix}0.008\\ 0.024\end{bmatrix}\mu^{-0.46}\bar{c}_{z_{sep}}^{-0.57},\ \begin{bmatrix}0.0055\\ 0.014\end{bmatrix}\bar{P}_{SOL}^{1.18}\,\mu^{-1.42}\right)\right). \tag{45}$$

Appendix B. Control synthesis and stability analysis

The following is a derivation of the control laws (30)–(33) presented in section 4.2. Controlling the dynamics of $\tilde{n}_D$ and $\tilde{n}_T$ is equivalent to controlling the dynamics of $\tilde{\gamma}=\gamma-\bar{\gamma}$ and $\tilde{n}=n-\bar{n}$. Using (27)–(29) along with the definitions for the tritium fraction ($\gamma=n_T/n_{DT}$) and the total plasma density ($n=n_i+n_e$), the dynamics of $\tilde{\gamma}$ and $\tilde{n}$ are determined to be

$$\begin{aligned}\dot{\tilde{\gamma}} = \dot{\gamma} &= \frac{\dot{n}_T n_{DT}-n_T\dot{n}_{DT}}{n_{DT}^2} = \frac{\dot{n}_T}{n_{DT}}-\gamma\frac{\dot{n}_{DT}}{n_{DT}} \\ &= \frac{1}{n_{DT}}\left[\dot{n}_T-\gamma\left(\dot{n}_D+\dot{n}_T\right)\right] \\ &= \frac{1}{n_{DT}}\left[-\frac{n_T}{\tau_T}-S_\alpha+\gamma\Gamma_{DT_s}+S_T \right. \\ &\quad \left. -\gamma\left(-\frac{n_T}{\tau_T}-\frac{n_D}{\tau_D}-2S_\alpha+S_D+S_T+\Gamma_{DT_s}\right)\right],\end{aligned} \tag{46}$$

$$\begin{aligned}\dot{\tilde{n}} = \dot{n} &= 2\dot{n}_D+2\dot{n}_T+3\dot{n}_\alpha+(Z_z+1)\,\dot{n}_z \\ &= -3\frac{n_\alpha}{\tau_\alpha}-2\frac{n_T}{\tau_T}-2\frac{n_D}{\tau_D}-S_\alpha+2S_D+2S_T+2\Gamma_{DT_s} \\ &\quad +3\Gamma_{\alpha_s}+(Z_z+1)\,c_{z_{core}}\dot{n}_e.\end{aligned} \tag{47}$$

Control laws for $P_{aux,i}$, $P_{aux,e}$, S_D, and S_T are derived from the Lyapunov function

$$V = k_i^2\tilde{E}_i^2+k_e^2\tilde{E}_e^2+k_\gamma^2\tilde{\gamma}^2+\tilde{n}^2, \tag{48}$$

and its time derivative

$$\dot{V} = k_i^2\tilde{E}_i\dot{\tilde{E}}_i+k_e^2\tilde{E}_e\dot{\tilde{E}}_e+k_\gamma^2\tilde{\gamma}\dot{\tilde{\gamma}}+\tilde{n}\dot{\tilde{n}}, \tag{49}$$

where k_i, k_e, and k_γ are positive constants [7]. The substitution of the dynamics for $\dot{\tilde{E}}_i$, $\dot{\tilde{E}}_e$, $\dot{\tilde{\gamma}}$, and $\dot{\tilde{n}}$ (defined by (25), (26), (46) and (47)) into (49) gives

$$\begin{aligned}\dot{V} = {} & k_i^2\tilde{E}_i\left[P_{aux,i}-\frac{\bar{E}_i}{\tau_{E,i}}-\frac{\tilde{E}_i}{\tau_{E,i}}+\phi_\alpha P_\alpha+P_{ei}\right] \\ & +k_e^2\tilde{E}_e\left[P_{aux,e}-\frac{\bar{E}_e}{\tau_{E,e}}-\frac{\tilde{E}_e}{\tau_{E,e}}+(1-\phi_\alpha)\,P_\alpha-P_{ei}-P_{rad}+P_{ohm}\right] \\ & +\frac{k_\gamma^2}{n_{DT}}\tilde{\gamma}\left[S_T-S_\alpha-\frac{n_T}{\tau_T}+\gamma\Gamma_{DT_s}\right. \\ & \left.-\gamma\left(S_D+S_T-\frac{n_D}{\tau_D}-\frac{n_T}{\tau_T}-2S_\alpha+\Gamma_{DT_s}\right)\right] \\ & +\tilde{n}\left[2S_D+2S_T-3\frac{n_\alpha}{\tau_\alpha}-2\frac{n_T}{\tau_T}-2\frac{n_D}{\tau_D}\right. \\ & \left.-S_\alpha+2\Gamma_{DT_s}+3\Gamma_{\alpha_s}+(Z_z+1)\,c_{z_{core}}\dot{n}_e\right].\end{aligned} \tag{50}$$

Substitution of the control laws for $P_{aux,i}$ (30), $P_{aux,e}$ (31), S_D (32), and S_T (33) render the inequality

$$\dot{V} = -\frac{k_i^2\tilde{E}_i^2}{\tau_{E,i}}-\frac{k_e^2\tilde{E}_e^2}{\tau_{E,e}}-K_T\frac{k_\gamma^2\tilde{\gamma}^2}{n_{DT}}-K_N\tilde{n}^2\leqslant 0, \tag{51}$$

true such that the system (25)–(29) is driven to the desired references.

The following shows that bringing the deviations $\tilde{\gamma}$, $\tilde{n}$, $\tilde{E}_i$, and $\tilde{E}_e$ to zero also brings $\tilde{n}_\alpha$ to zero ($\tilde{n}_\alpha\to 0$). Consider the Lyapunov function V_α, its time derivative, and (27):

$$V_\alpha = \frac{\tilde{n}_\alpha^2}{2}, \tag{52}$$

$$\dot{V}_\alpha = \tilde{n}_\alpha\left(-\frac{n_\alpha}{\tau_\alpha}+S_\alpha+\Gamma_{\alpha_s}\right)\equiv\tilde{n}_\alpha\Upsilon, \tag{53}$$

where Υ increases with decreasing n_α and vice versa. If μ is a positive continuous function, then $\Upsilon=-\mu\tilde{n}_\alpha$ is valid and the statement

$$\dot{V}_\alpha = -\mu\tilde{n}_\alpha^2<0\quad\forall\quad\tilde{n}_\alpha\neq 0, \tag{54}$$

when $\tilde{E}_i=\tilde{E}_e=\tilde{\gamma}=\tilde{n}=0$ shows that $\tilde{n}_\alpha$ is driven to zero.

Appendix C. Actuator allocation and dynamics

For the burn control problem presented in this work, actuator allocation is not needed for the external DT fueling because there are two pellet injectors ($S_{D_{pel}}$ and $S_{DT_{pel}}$) and two control requests for fueling (S_D and S_T). Therefore, the values of $S_{D_{pel}}$ and $S_{DT_{pel}}$ needed to satisfy the fueling control laws (32) and (33) can be immediately determined using (19) and (20). In contrast, an actuator allocator will be needed to map the ITER's suite of auxiliary power actuators to the control laws for external heating (30) and (31). The auxiliary power delivered to the ions $P_{aux,i}$ and the electrons $P_{aux,e}$ is given by

$$P_{aux,i} = \eta_{ic}\phi_{ic}P_{ic}+\eta_{ec}\phi_{ec}P_{ec}+\eta_{nb}\phi_{nb}P_{nb}, \tag{55}$$

$$P_{aux,e} = \eta_{ic}\bar{\phi}_{ic}P_{ic}+\eta_{ec}\bar{\phi}_{ec}P_{ec}+\eta_{nb}\bar{\phi}_{nb}P_{nb}, \tag{56}$$

where P_{ic}, P_{ec}, and P_{nb} are the the power output of the ion cyclotron systems, the electron cyclotron systems, and the neutral beam injectors. The fractions of the actuator powers delivered to the plasma's ions are ϕ_{ic}, ϕ_{ec}, and ϕ_{nb}, while $\bar{\phi}_{ic}$, $\bar{\phi}_{ec}$, and $\bar{\phi}_{nb}$ are the fractions delivered to the plasma's electrons. Overall actuator efficiencies are given by η_{ic}, η_{ec}, and η_{nb}.

In [8], the mapping between the control requests and the actuator outputs (e.g. (55) and (56)) was solved by posing the actuator allocation problem as a strictly convex quadratic program with a unique optimal solution. In [9], this actuator allocator design was compared to an adaptive design based on dynamic update laws, removing the requirement of solving an optimization problem at every time step. This adaptive actuator allocator was designed to overcome the existence of uncertain actuator dynamics. The particular actuator dynamics consider in [9] were first-order lags with uncertain time constants. This can be represented by

$$\tau \frac{dy}{dt} + y = x, \tag{57}$$

where $x(t)$ is the actuator command given by the actuator allocator, $y(t)$ is the lagged actuator output, and τ is the uncertain time constant. The simulation study presented in [9] showed good control performance in the presence of slow, uncertain actuator dynamics. This adaptive actuator allocation design was improved upon in [10] by including compensation for the following time-varying and state-dependent parameters (which included uncertainty): the thermalization delay of the neutral beam particles, the fractions of neutral beam power deposited into the plasma's ion and electron populations, and the temperature-dependent fueling efficiencies of the pellet injectors.

ORCID iD

Vincent Graber https://orcid.org/0000-0003-2058-2258

References

[1] Humphreys D. *et al* 2015 Novel aspects of plasma control in ITER *Phys. Plasmas* **22** 021806

[2] Schuster E., Krstić M. and Tynan G. 2003 Burn control in fusion reactors via nonlinear stabilization techniques *Fusion Sci. Technol.* **43** 18–37

[3] Boyer M. and Schuster E. 2015 Nonlinear burn condition control in tokamaks using isotopic fuel tailoring *Nucl. Fusion* **55** 083021

[4] Boyer M. and Schuster E. 2014 Nonlinear control and online optimization of the burn condition in ITER via heating, isotopic fueling and impurity injection *Plasma Phys. Control. Fusion* **56** 104004

[5] Boyer M. and Schuster E. 2012 Adaptive nonlinear burn control in tokamak fusion reactors *American Control Conf.* (*Montreal, Canada*, *27–29 June*) (https://doi.org/10.1109/ACC.2012.6315530)

[6] Pacher G., Pacher H.D., Janeschitz G. and Kukushkin A.S. 2008 ITER operation window determined from mutually consistent core–SOL–divertor simulations: definition and application *Nucl. Fusion* **48** 105003

[7] Khalil H. 2001 *Nonlinear Systems* 3rd edn (Prentice Hall)

[8] Graber V. and Schuster E. 2020 Nonlinear adaptive burn control and optimal control allocation of over-actuated two-temperature plasmas *American Control Conf.* (*Denver, USA*, *01–03July*) (https://doi.org/10.23919/ACC45564.2020.9147885)

[9] Graber V. and Schuster E. 2022 Nonlinear burn control in ITER using adaptive allocation of actuators with uncertain dynamics *Nucl. Fusion* **62** 026016

[10] Graber V. and Schuster E. 2022 Actuator allocation with adaptive estimation of time-varying uncertain parameters for nonlinear burn control *2022 IEEE Conf. on Control Technology and Applications (CCTA)* (*Trieste, Italy*, *23–25August*) pp 845–50

[11] Vitela J.E. 2007 Burn control of a two-temperature tokamak power plant with online estimations of particle and energy transport losses *Fusion Sci. Technol.* **52** 1–28

[12] Pacher H.D., Kukushkin A.S., Pacher G.W., Kotov V., Pitts R.A. and Reiter D. 2015 Impurity seeding in ITER DT plasmas in a carbon-free environment *J. Nucl. Mater.* **463** 591–5

[13] Graber V. and Schuster E. 2021 Assessment of the burning-plasma operational space in ITER by using a control-oriented core-SOL-divertor model *Fusion Eng. Des.* **171** 112516

[14] Graber V. and Schuster E. 2023 Control-oriented core-SOL-divertor model to address integrated burn and divertor control challenges in ITER *Fusion Eng. Des.* **192** 113635

[15] Stangeby P. 2000 *The Plasma Boundary* (IOP)

[16] Shimada M. *et al* 2007 Chapter 1: Overview and summary *Nucl. Fusion* **47** S1–S17

[17] Mantsinen M. and Salomaa R. 1997 *Simulations of Burn Dynamics in Tokamak Fusion Reactors* (Helsinki University of Technology)

[18] Meade D. *et al* 2002 Exploration of burning plasmas in FIRE *19th Fusion Energy Conf. (IAEA)* (*Lyon, France*, *14–19October*) (available at: https://www-pub.iaea.org/mtcd/publications/pdf/csp_019c/pdf/ft2_6.pdf)

[19] Yamazaki K., Higashiyama Y., Sawafuji T., Sakawa Y., Arimoto H., Shoji T., Garcia J., Dies J., Igitkhanov Y. and Dolan T.J. 2006 Burning plasma simulation of TR-1 tokamak and HR-1 helical reactors *Fusion Eng. Des.* **81** 2743–8

[20] Houlberg W., Attenberger S. and Hively L. 1982 Contour analysis of fusion reactor plasma performance *Nucl. Fusion* **22** 935

[21] Rodriguez-Fernandez P. *et al* 2022 Overview of the SPARC physics basis towards the exploration of burning-plasma regimes in high-field, compact tokamaks *Nucl. Fusion* **62** 042003

[22] Martinell J. and Vitela J. 2016 An optimal burn regime in a controlled tokamak fusion power plant *IEEE Trans. Plasma Sci.* **44** 296–305

[23] Jakobs M., Cardozo N.L. and Jaspers R. 2014 Fusion burn equilibria sensitive to the ratio between energy and helium transport *Nucl. Fusion* **54** 122005

[24] Graber V. and Schuster E. 2019 Tritium-concentration requirements in the fueling lines for high-Q operation in ITER *46th EPS Conf. on Plasma Physics* (*Milan, Italy*, *8–12July*) (European Physical Society) (available at: https://www6.lehigh.edu/~eus204/per/publications/abstracts/eps19a.pdf)

[25] Snipes J. *et al* 2012 Actuator and diagnostic requirements of the ITER plasma control system *Fusion Eng. Des.* **87** 1900–6

[26] Adetola V. and Guay M. 2006 Adaptive output feedback extremum seeking receding horizon control of linear systems *J. Process Control* **16** 521–33

[27] Guay M. and Zhang T. 2003 Adaptive extremum seeking control of nonlinear dynamic systems with parametric uncertainties *Automatica* **39** 1283–93
[28] Adetola V. and Guay M. 2006 Excitation signal design for parameter convergence in adaptive control of linearizable systems *Proc. 45th IEEE Conf. on Decision and Control* (*San Diego, CA, USA*, *13–15 December*) pp 447–52
[29] Shimada M. *et al* 2000 Physics design of ITER-FEAT *Plasma and Fusion Research* (*Toki, Gifu, Japan*, *18–22January*) vol 3 pp 77–83 (available at: https://dl.ndl.go.jp/view/prepareDownload?itemId=info:ndljp/pid/11127353&bundleNo=1&contentNo=1)
[30] Harvey R., Nevins W.M., Smith G.R., Lloyd B., O'Brien M.R. and Warrick C.D. 1997 Electron cyclotron heating and current drive in ITER *Nucl. Fusion* **37** 69–81
[31] Bosch H. and Hale G. 1992 Improved formulas for fusion cross-sections and thermal reactivities *Nucl. Fusion* **32** 611–31
[32] Wesson J. 1997 *Tokamaks* 2nd edn (Clarendon)
[33] Gallart D., Mantsinen M. and Kazakov Y. 2015 Modelling of ICRF heating in DEMO with special emphasis on bulk ion heating *AIP Conf. Proc.* **1689** 060004
[34] Gross R. 1984 *Fusion Energy* (Wiley)
[35] Combs S., Baylor L.R., Meitner S.J., Caughman J.B.O., Rasmussen D.A. and Maruyama S. 2012 Overview of recent developments in pellet injection for ITER *Fusion Eng. Des.* **87** 634–40
[36] Martin Y.R. and Takizuka T. (The ITPA CDBM H-mode Threshold Database Working Group) 2008 Power requirement for accessing the H-mode in ITER *J. Phys.: Conf. Ser.* **123** 012033
[37] Greenwald M. 2002 Density limits in toroidal plasmas *Plasma Phys. Control. Fusion* **44** R27
[38] Li W., Li B., Maruyama S., Jiang T., Yang Y., Xia Z.W., Zhang Y.X. and Lu J. 2012 A description of the ITER's gas injection systems and current R&D activities *Fusion Eng. Des.* **87** 813–21
[39] Pajares A. and Schuster E. 2019 Robust nonlinear burn control in ITER to handle uncertainties in the fuel-line concentrations *Nucl. Fusion* **59** 096023
[40] Johansen T. and Fossen T. 2013 Control allocation—a survey *Automatica* **49** 1087–103
[41] Kukushkin A., Pacher H.D., Kotov V., Reiter D., Coster D.P. and Pacher G.W. 2007 Effect of the dome on divertor performance in ITER *J. Nucl. Mater.* **363–365** 308–13